# Time-delayed nonsequential double ionization with few-cycle laser pulses: Importance of the carrier-envelope phase

C. Figueira de Morisson Faria,[1] T. Shaaran,[1,2] and M. T. Nygren[1,3]

[1]*Department of Physics and Astronomy, University College London, Gower Street, London WC1E 6BT, United Kingdom*

[2]*ICFO-Institut de Ciències Fotòniques, Avenida Carl Friedrich Gauss, 308860 Castelldefels (Barcelona), Spain*

[3]*Theoretical Physics Group, Imperial College London, South Kensington Campus, London SW7 2AZ, United Kingdom*

We perform theoretical investigations of laser-induced nonsequential double ionization with few-cycle pulses, with particular emphasis on the dependence of the electron-momentum distributions on the carrier-envelope phase. We focus on the recollision-excitation with subsequent tunneling ionization (RESI) pathway, in which a released electron, upon return to its parent ion, gives part of its kinetic energy to promote a second electron to an excited state. At a subsequent time, the second electron is freed through tunneling ionization. We show that the RESI electron-momentum distributions vary dramatically with regard to the carrier-envelope phase. By performing a detailed analysis of the dynamics of the two active electrons in terms of quantum orbits, we relate the shapes and the momentum regions populated by such distributions to the dominant set of orbits along which rescattering of the first electron and ionization of the second electron occurs. These orbits can be manipulated by varying the carrier-envelope phase. This opens a wide range of possibilities for controlling correlated attosecond electron emission by an adequate pulse choice.

PACS number(s): 32.80.Rm

## I. INTRODUCTION

Ultrashort laser pulses with durations of a few optical cycles can reach very high intensities and still carry much less energy than their longer counterparts [1]. This enables a wide range of applications, such as controlling the collective electron motion in condensed matter [2], manipulating chemical reactions [3], and generating isolated XUV attosecond pulses [4,5]. In this pulse-length regime, the carrier-envelope phase (CEP), that is, the phase of the carrier frequency with respect to the pulse envelope, dramatically influences strong-field phenomena, such as high-harmonic generation (HHG) [1], above-threshold ionization (ATI) [6], and laser-induced nonsequential double ionization (NSDI). Specifically for NSDI, it has been shown that the electron-momentum distributions change their shapes considerably when this parameter varies. In fact, asymmetric electron momentum distributions have been identified both theoretically [7–12] and experimentally [13–15] for NSDI with few-cycle driving pulses. Most of these studies have focused on the electron-impact ionization pathway, in which the second electron has enough energy to overcome the second ionization potential and both electrons reach the continuum simultaneously.

In recent experiments, however, a similar effect has also been observed in a parameter range for which another NSDI pathway is prevalent: Recollision excitation with subsequent tunneling ionization (RESI) [14,15]. RESI happens when the first electron, upon its return to the core, promotes the second electron to an excited bound state, from which, with laser assistance, it subsequently tunnels [16]. In RESI, the first electron leaves immediately upon rescattering, while the second electron tunnel ionizes near the subsequent field maximum. Hence, there is a time delay between rescattering of the first electron and tunnel ionization of the second electron. For a comprehensive discussion of RESI, see our recent review [17].

The above-mentioned experimental evidence shows asymmetric electron momentum distributions, as functions of the momentum components $p_{1\parallel}, p_{2\parallel}$ parallel to the laser-field polarization, whose shape varies dramatically with the CEP. For instance, in Ref. [15] asymmetric distributions have been observed, whose probability densities, depending on this phase, are either stronger in the positive half axes $p_{i\parallel} = 0$, $p_{j\parallel} \geqslant 0$, with $i, j = 1, 2$ and $i \neq j$, or in the negative half axes $p_{i\parallel} = 0$, $p_{j\parallel} \leqslant 0$, defined in the parallel-momentum plane $p_{1\parallel} p_{2\parallel}$. As the CEP is varied, the momentum region in which the correlated probability density is larger shifts from one half axis to the other. This behavior resembles to a great extent that observed for electron-impact ionization [13], which has been explained by us in previous work in terms of a shift in the dominant set of orbits along which inelastic rescattering occurs [7,8]. The main difference is that, instead of being located either at the positive or negative momentum half axes mentioned above, the electron-impact NSDI distributions populated either the first or the third quadrant of the $p_{1\parallel} p_{2\parallel}$ plane. Depending on the CEP range chosen, they shifted from the first to the third quadrant of the parallel-momentum plane, or vice versa.

In the present work, we address the question whether, similarly to what happens in the direct pathway, it is possible to associate dominant sets of trajectories to specific values of the CEP and to specific shapes of the electron-momentum distributions. For that purpose, we apply the analytical RESI model developed by us in previous publications [18,19] to few-cycle pulses of different CEPs. In this model, the Feynman diagram corresponding to RESI has been considered from the outset, and the pertaining transition amplitude has been calculated in the strong-field approximation using the steepest descent method. A particularly important issue in the context of RESI with few-cycle driving pulses is that particular care must be taken with regard to causality if the above-mentioned methods are used. This issue has been addressed by us in a recent publication [20].

This article is organized as follows. In Sec. II, we provide a brief summary of the method developed in Refs. [18,19].

In Sec. III, we determine the dominant sets of orbits for the first and second electrons from the solutions of the saddle-point equations. Subsequently, in Sec. IV we compute the RESI electron-momentum distributions and analyze their CEP dependence in terms of such orbits. Finally, in Sec. V we state the main conclusions to be drawn from this work.

## II. MODEL

### A. Transition amplitude

Within the strong-field approximation, the transition amplitude corresponding to RESI reads [18]

$$M(\mathbf{p}_1, \mathbf{p}_2) = \int_{-\infty}^{\infty} dt \int_{-\infty}^{t} dt' \int_{-\infty}^{t'} dt'' \int d^3k$$
$$\times V_{\mathbf{p}_2 e} V_{\mathbf{p}_1 e, \mathbf{k}g} V_{\mathbf{k}g} \exp[i S(\mathbf{p}_1, \mathbf{p}_2, \mathbf{k}, t, t', t'')]. \quad (1)$$

In Eq. (1),

$$S(\mathbf{p}_1, \mathbf{p}_2, \mathbf{k}, t, t', t'')$$
$$= E_1^{(g)} t'' + E_2^{(g)} t' + E_2^{(e)} (t - t') - \int_{t''}^{t'} \frac{[\mathbf{k} + \mathbf{A}(\tau)]^2}{2} d\tau$$
$$- \int_{t'}^{\infty} \frac{[\mathbf{p}_1 + \mathbf{A}(\tau)]^2}{2} d\tau - \int_{t}^{\infty} \frac{[\mathbf{p}_2 + \mathbf{A}(\tau)]^2}{2} d\tau \quad (2)$$

gives the semiclassical action, while

$$V_{\mathbf{k}g} = \langle \tilde{\mathbf{k}}(t'') | V | \psi_1^{(g)} \rangle$$
$$= \frac{1}{(2\pi)^{3/2}} \int d^3r_1 V(\mathbf{r}_1) e^{-i\tilde{\mathbf{k}}(t'') \cdot \mathbf{r}_1} \psi_1^{(g)}(\mathbf{r}_1), \quad (3)$$

$$V_{\mathbf{p}_1 e, \mathbf{k}g} = \langle \tilde{\mathbf{p}}_1(t'), \psi_2^{(e)} | V_{12} | \tilde{\mathbf{k}}(t'), \psi_2^{(g)} \rangle$$
$$= \frac{1}{(2\pi)^3} \iint d^3r_2 d^3r_1 \exp[-i(\mathbf{p}_1 - \mathbf{k}) \cdot \mathbf{r}_1]$$
$$\times V_{12}(\mathbf{r}_1, \mathbf{r}_2) \left[\psi_2^{(e)}(\mathbf{r}_2)\right]^* \psi_2^{(g)}(\mathbf{r}_2), \quad (4)$$

and

$$V_{\mathbf{p}_2 e} = \langle \tilde{\mathbf{p}}_2(t) | V_{\text{ion}} | \psi_2^{(e)} \rangle$$
$$= \frac{1}{(2\pi)^{3/2}} \int d^3r_2 V_{\text{ion}}(\mathbf{r}_2) e^{-i\tilde{\mathbf{p}}_2(t) \cdot \mathbf{r}_2} \psi_2^{(e)}(\mathbf{r}_2). \quad (5)$$

are the form factors related to the ionization of the first electron, recollision of the first electron with excitation of the second electron, and tunnel ionization of the second electron [Eqs. (3)–(5), respectively]. These form factors provide information about the binding potential $V(\mathbf{r}_1)$ and $V_{\text{ion}}(\mathbf{r}_2)$ "seen" by the first and the second electrons, respectively, and about the interaction $V_{12}(\mathbf{r}_1, \mathbf{r}_2)$ of the first electron with the core.

Equation (1) describes a process in which the first electron, initially bound in the ground state $|\psi_1^{(g)}\rangle$ with energy $E_1^{(g)}$, is freed by tunnel ionization at time $t''$ into a Volkov state $|\tilde{\mathbf{k}}(t'')\rangle$. Thereafter, it propagates in the continuum from the time $t''$ to the time $t'$ with intermediate momentum $\mathbf{k}$. At a time $t'$, it rescatters inelastically with the core and, through the interaction $V_{12}$, excites a second electron from the ground state $|\psi_2^{(g)}\rangle$ of the singly ionized target to the state $|\psi_2^{(e)}\rangle$. The energies of the ground and excited states of the singly ionized target are $E_2^{(g)}$ and $E_2^{(e)}$, respectively. The first electron reaches the detector with final momentum $\mathbf{p}_1$ immediately after rescattering. The second electron remains bound until a later

time $t$, when it is released by tunnel ionization into a Volkov state $|\tilde{\mathbf{p}}_2(t)\rangle$. It reaches the detector with final momentum $\mathbf{p}_2$. In the above-stated equations, $\tilde{\mathbf{k}}(\tau) = \mathbf{k} + \mathbf{A}(\tau)$ and $\tilde{\mathbf{p}}_n(\tau) = \mathbf{p}_n + \mathbf{A}(\tau)(\tau = t, t', t'')$ in the length gauge, and $\tilde{\mathbf{k}}(\tau) = \mathbf{k}$ and $\tilde{\mathbf{p}}_n(\tau) = \mathbf{p}_n$ in the velocity gauge, with $n = 1, 2$. In Ref. [18], we have verified that, in practice, the results obtained in both gauges are nearly identical [21].

### B. Saddle-point equations

The transition amplitude (1) is computed using the steepest descent method. Hence, one must find the values of $t, t', t''$ and $\mathbf{k}$ for which the action (2) is stationary, that is, for which $\partial_{t''} S(\mathbf{p}_1, \mathbf{p}_2, \mathbf{k}, t, t', t'') = \partial_{t'} S(\mathbf{p}_1, \mathbf{p}_2, \mathbf{k}, t, t', t'') = \partial_t S(\mathbf{p}_1, \mathbf{p}_2, \mathbf{k}, t, t', t'') = 0$, and $\partial_{\mathbf{k}} S(\mathbf{p}_1, \mathbf{p}_2, \mathbf{k}, t, t', t'') = \mathbf{0}$. For details on this method see Ref. [22].

The conditions upon $t''$, $\mathbf{k}$, and $t'$ give the saddle-point equations

$$[\mathbf{k} + \mathbf{A}(t'')]^2 = -2E_1^{(g)}, \quad (6)$$

$$\mathbf{k} = -\frac{1}{t' - t''} \int_{t''}^{t'} d\tau \mathbf{A}(\tau), \quad (7)$$

and

$$[\mathbf{p}_1 + \mathbf{A}(t')^2] = [\mathbf{k} + \mathbf{A}(t')]^2 - 2\left(E_2^{(g)} - E_2^{(e)}\right), \quad (8)$$

while the condition upon $t$ leads to

$$[\mathbf{p}_2 + \mathbf{A}(t)]^2 = -2E_2^{(e)}. \quad (9)$$

Equation (6) expresses the fact that the energy of the first electron is conserved at the instant $t''$ at which tunneling ionization occurs. Equation (7) fixes the intermediate momentum of the first electron in order to guarantee its return to its parent ion. Equation (8) states that, upon rescattering, the first electron transferred a fraction $E_{\text{exc}} = E_2^{(g)} - E_2^{(e)}$ of its kinetic energy $[\mathbf{k} + \mathbf{A}(t')]^2/2$ upon return and reached the detector with final kinetic energy $[\mathbf{p}_1 + \mathbf{A}(t')]^2/2$. Finally, Eq. (9) gives the energy conservation for the second electron upon tunneling, which reaches the detector with final momentum $\mathbf{p}_2$. Note that Eqs. (6) and (9) have no real solution, since tunneling has no classical counterpart. If written in terms of the electron momentum components $(p_{n\parallel}, p_{n\perp})$, $n = 1, 2$ parallel and perpendicular to the laser-field polarization, Eqs. (8) and (9) give the kinematic constraints related to the first and second electrons, respectively. These constraints have been discussed in detail in Refs. [18,19] and [20] for monochromatic fields and few-cycle pulses, respectively, and are briefly mentioned here.

Explicitly, from Eq. (8) one obtains the condition

$$-A(t') - \sqrt{2\triangle E} \leqslant p_{1\parallel} \leqslant -A(t') + \sqrt{2\triangle E}, \quad (10)$$

where $\triangle E = E_{\text{kin}}(t', t'') - \tilde{E}_{\text{exc}}$ denotes the energy difference between the kinetic energy $E_{\text{kin}}(t', t'')$ of the first electron upon return and the energy $\tilde{E}_{\text{exc}} = E_{\text{exc}} + p_{1\perp}^2/2$. The latter is an effective excitation energy, which increases with perpendicular momentum $p_{1\perp}$. Inside the boundaries defined by Eq. (10), rescattering has a classical counterpart and the probability density associated with it is significant, while, outside those boundaries, rescattering is not classically allowed to occur and the corresponding probability density is vanishingly small. The

largest region is obtained for vanishing transverse momentum $p_{1\perp}$.

This implies that (i) the region in the parallel momentum plane determined by rescattering of the first electron is centered around $p_{1\parallel} = -A(t')$, where $A(t')$ is the vector potential at the time the first electron returns, and (ii) the extension of this region is determined by the energy difference $\triangle E$. In order to draw upper bounds for such momentum regions, it is useful to assume that $p_{1\perp} = 0$ and consider the maximal kinetic energy $E_{\mathrm{kin}}^{\max}(t',t'')$ the first electron may have upon return. If $E_{\mathrm{kin}}^{\max}(t',t'') \gg E_{\mathrm{exc}}$, this region will be very large. In contrast, if $E_{\mathrm{kin}}^{\max}(t',t'') \simeq E_{\mathrm{exc}}$, the energy of the returning electron will be just enough to excite the second electron. Hence, the momentum it will have subsequently to the collision will be that acquired from the field at the instant of rescattering. In terms of momentum-space constraints, this means that the region in the parallel momentum plane will collapse around $p_{1\parallel} = -A(t')$.

For a monochromatic field, $A(t') = \pm 2\sqrt{U_p}$ and $E_{\mathrm{kin}}^{\max}(t',t'') = 3.17 U_p$ [19]. However, for a few-cycle pulse, $-A(t')$ and $E_{\mathrm{kin}}^{\max}(t',t'')$ will depend on the rescattering event within the pulse. This means that each specific rescattering event will lead to a region in the $p_{1\parallel} p_{2\parallel}$ plane, whose extension and center depend on the electron return time and kinetic energy for a particular set of orbits.

Similarly, Eq. (9) can be rewritten as

$$[p_{2\parallel} + A(t)]^2 = -2E_2^{(e)} - p_{2\perp}^2. \tag{11}$$

The above-stated expression shows that there will be a large drop in the yield with increasing transverse momentum, as $\mathbf{p}_{2\perp}$ effectively widens the potential barrier through which the second electron must tunnel. The electron tunnels most probably at the laser field maxima, for which $A(t) \ll 1$ and $p_{2\parallel} \simeq 0$. Hence, the momentum-space conditions for which ionization of the second electron is most probable lie approximately at $(p_{2\parallel}, p_{2\perp}) = (0,0)$. For a few-cycle pulse, depending on the specific tunnel ionization event, the barrier will be narrower or wider.

In summary, the constraints upon the momentum of the second electron determine the position of the cross-shaped distributions at the axes $p_{n\parallel} = 0$ in the parallel-momentum plane, while those related to the momentum of the first electron determine the regions along these axes that will be populated, that is, whether they will be long or short. Clearly, for a few-cycle pulse this length will vary with each particular event.

## III. RELEVANT IONIZATION AND RESCATTERING EVENTS

In this section, we identify the dominant ionization and rescattering channels for the first electron and the relevant tunneling events for the second electron. We provide a simplified, intuitive discussion, based on a direct analysis of the pulse and also state the main results obtained from the solution of the saddle-point equations. For a detailed quantum-orbit analysis, we refer to the Appendix.
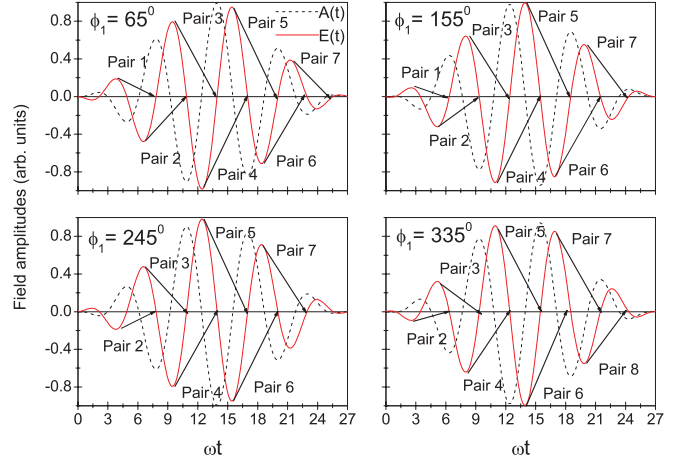


FIG. 1. (Color online) Schematic representation of the electric field $\mathbf{E}(t)$ and the corresponding vector potential $\mathbf{A}(t)$, for a short pulse of $N = 4.3$ cycles, whose shape is defined by Eq. (12) and whose CEPs are the same as in the previous figure. The arrows indicate the approximate classical times around which the *first* electron leaves, in case it returns at a field crossing. The pairs of orbits are indicated by the labels Pair $n$, where $n$ ranges from 1 to 8. The fields have been normalized to $E(t)/E_0$ and $A(t)/A_0$, where $E_0$, $A_0$ denote the field amplitudes. The CEPs are $\phi_1 = 65°(\phi = 5°)$, $\phi_1 = 155°(\phi = 95°)$, $\phi_1 = 245°(\phi = 185°)$, and $\phi_1 = 335°(\phi = 275°)$.

We employ the linearly polarized few-cycle pulse $\mathbf{E}(t) = -\partial_t \mathbf{A}(t)/dt$, where the vector potential $\mathbf{A}(t)$ is given by

$$\mathbf{A}(t) = 2\sqrt{U_p} \sin^2\left(\frac{\omega t}{2N}\right)\sin(\phi + \omega t)\hat{e}_z. \tag{12}$$

In Eq. (12), $N$ denotes the number of cycles in the pulse, $\omega$ is the field frequency, $\phi$ is the CEP, $U_p = E_0^2/(4\omega^2)$ is the ponderomotive energy, $E_0$ is the field amplitude, and $\hat{e}_z$ is the polarization vector. Throughout, we choose the number of cycles as $N = 4.3$ and $\phi = \phi_1 - \phi_0$, where $\phi_0 = 60°$ is an offset value. This is well within the parameter range employed in experiments [15]. Throughout, we refer to the phase $\phi_1$ without the offset value to facilitate a comparison with the existing literature. The bound-state energies taken correspond to argon. Initially, both electrons are bound in the $3p$ state. The first electron recollides with the core, exciting a second electron to the $4s$ state.

### A. Approximate ionization and rescattering times

We now identify the relevant sets of orbits for the pulse (12). In Fig. 1, we indicate the approximate ionization and rescattering times for the first electron for the values of the CEP employed in this article. These sets of times are associated with the real part of the complex times $t''$ and $t'$, obtained from the solutions of the saddle-point equations (6)–(8). Such solutions always occur in pairs, which, physically, correspond to the fact that the first electron may return along a shorter and a longer orbit. In the figure, one may identify up to eight pairs of orbits, whose ionization and rescattering times vary with the CEP. In the following, we refer to these pairs as Pair $n(e_1)$, with $n = 1, \ldots, 8$. For each pair, the electron will leave most probably at a local maximum and return most probably at the subsequent crossing. The most relevant pairs are those
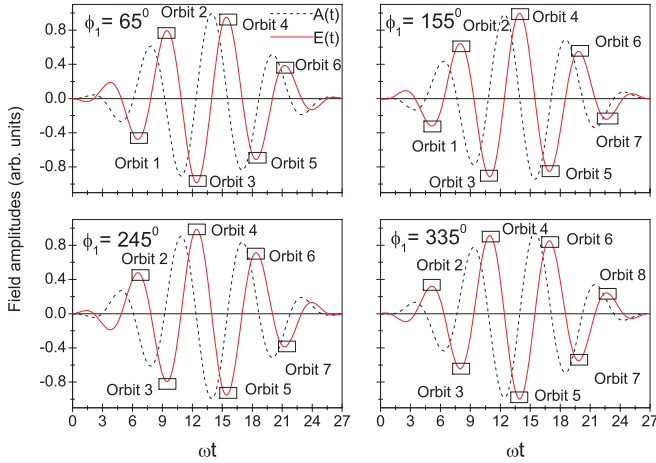
FIG. 2. (Color online) Schematic representation of the same electric field $\mathbf{E}(t)$ and the corresponding vector potential $\mathbf{A}(t)$ as in the previous figures, but highlighting the times around which ionization of the *second* electron is expected to occur, indicated by the squares in the figure. The orbits are indicated by the labels Orbit $n$, where $n$ ranges from 1 to 8. The fields have been normalized to $E(t)/E_0$ and $A(t)/A_0$, where $E_0$, $A_0$ denote the field amplitudes.

near the center of the pulse, as the field intensity in this case is higher.

Figure 2 shows the approximate times at which the second electron tunnels. These times are located around the field maxima and also strongly depend on the CEP. The corresponding orbits will be referred to as Orbit $n(e_2)$, with $n$ ranging from 1 to 8. Once more, the orbits for which tunneling is expected to be most prominent are close to the center of the pulse. Note that the second electron cannot tunnel from an excited state before the first electron rescatters. This implies that, for instance, ionization related to Orbit $2(e_2)$ can only be caused by Pair $1(e_1)$, or ionization related to Orbit $3(e_2)$ by Pairs $1(e_1)$ and $2(e_1)$. Even though this sounds obvious, a rigorous treatment of causality can be a nontrivial issue, especially within the context of the steepest descent method, and requires an extensive modification of the contours to be taken into account. For a detailed discussion, see our previous work [20].

### B. Solutions of the saddle-point equations

The times of the events sketched above can be associated to the real parts of the solutions of the saddle-point equations (6)–(9). The imaginary parts of such solutions give a rough measure of how "allowed," or "forbidden" a certain process is. For instance, for tunneling ionization of the first or second electron, the larger $\text{Im}[t'']$ and $\text{Im}[t]$ are, the wider the barrier the electron must tunnel and hence the less probable a specific event is. For the second electron, this imaginary part exhibits a minimum at vanishing momenta $p_{n\parallel} = 0$. This corresponds to the times for which the field is maximum. For the rescattering time of the first electron, $\text{Im}[t'] \simeq 0$ in the whole momentum region for which this process has a classical counterpart. This region is centered around $p_{1\parallel} = -A(t')$ and extends to higher and lower momenta according to the constraint (10). It is delimited by two solutions that nearly coalesce at the minimal and the maximal classically allowed momenta.

Hence, for the first electron, a pair of orbits will lead to dominant contributions in the electron-momentum distributions if (i) the corresponding potential barrier through which the electrons tunnel is as narrow as possible, as this will lead to a high ionization probability, and (ii) the kinetic energy of the first electron upon return is as high as possible, as this will populate a large region in momentum space. For the second electron, as there is no rescattering, a particular event will be dominant if (i) holds. Below we summarize our main findings for the first and second electrons for the specific pulses employed in this work.

For the first electron, Pairs $3(e_1)$ and $5(e_1)$ will populate mainly the negative momentum region $p_{1\parallel} < 0$, while Pair $4(e_1)$ will populate mostly the positive momentum region. Whether the origin $p_{1\parallel} = 0$ will or will not be included will depend on the driving-field intensity and on the specific event. Pair $3(e_1)$ is very important for $\phi_1 = 65°$, but loses relevance as the CEP increases. This is shown in the fact that $\text{Re}[t'']$ moves from the pulse center towards the pulse turn on, in an increase in $\text{Im}[t'']$ for this orbit and in a marked decrease in the classically allowed momentum region. Simultaneously, the contributions of Pair $4(e_1)$ remain relatively stable for the CEP range studied. This happens because both the kinetic energy acquired by the electron upon rescattering, that is, $-A(t')$, and the width of the potential barrier upon tunneling, roughly determined by $\text{Im}[t'']$, changes relatively little with the CEP. Physically, this happens because this specific ionization event lies in the central region of the pulse for the range of CEPS studied. Pair $5(e_1)$ increases in relevance as $\phi_1$ varies from $65°$ to $335°$. In this case, the corresponding ionization and rescattering times $\text{Re}[t'']$ and $\text{Re}[t']$ move from the turn off to the center of the pulse. There is a marked increase in the kinetic energy upon return, and hence in the classically allowed region. For this pair, $\text{Im}[t'']$ is comparable to that for Pair $4(e_1)$ over a wide range of phases. Hence, both pairs are expected to compete, until Pair $5(e_1)$ becomes the dominant channel.

For the second electron, we find that the dominant ionization channels are Orbits $4(e_2)$ and $5(e_2)$. This is expected as they are much closer to the center of the pulse, and, in terms of saddle-point solutions, this implies that the imaginary parts $\text{Im}[t]$ associated with these orbits are smaller than for the remaining channels. Interestingly, while for Orbit $4(e_2)$ this imaginary part remains stable as the CEP varies from $\phi_1 = 65°$ to $\phi_1 = 335°$, for Orbit $5(e_2)$ it decreases systematically. This means that the latter orbit increases in relevance. Physically, this is expected, as for Orbit $5(e_2)$, the real part $\text{Re}[t]$ of the saddle-point solution moves from the turn off to the center of the pulse.

A detailed analysis of the above-stated features, together with a thorough discussion of the kinetic energy of the electron upon return and plots of the saddle-point solutions, is provided in the Appendix.

### IV. ELECTRON-MOMENTUM DISTRIBUTIONS

In this section, we apply the information stated above in order to determine the regions in momentum space that should be occupied by the electron-momentum distributions. These predictions will be compared with the outcome of the actual computations, performed by setting $V_{\mathbf{p}_{1e},\mathbf{k}g} = \text{const.}$,
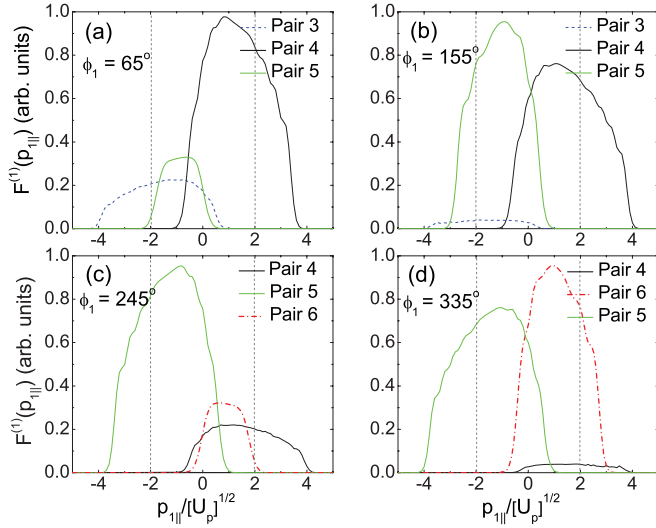
FIG. 3. (Color online) Partial electron momentum distributions $F^{(1)}(p_{1\parallel})$ [Eq. (13)] computed using the three most relevant individual ionization pathways for the first electron according to Fig. 1 and Table I for the same field and atomic parameters as in the previous figure. From left to right, the phases $\phi_1 = 65°$ [panel (a)], $\phi_1 = 155°$ [panel (b)], $\phi_1 = 245°$ [panel (c)], and $\phi_1 = 335°$ [panel (d)] have been taken. The probability densities have been normalized to slightly below unity for the dominant contributions in each panel, in order to facilitate a more direct comparison. The dotted lines in panels (a) to (d) indicate the momenta $p_{1\parallel} = \pm 2\sqrt{U_p}$, where the partial distributions related to a monochromatic driving field are expected to be peaked.

$V_{\mathbf{p}_2 e} = $ const. This guarantees that both the excitation and the ionization prefactors do not introduce any momentum bias, and the distributions represent the momentum constraints discussed in the previous section.

### A. Partial distributions

For simplicity, we commence by analyzing the partial momentum distributions

$$F^{(1)}(p_{1\parallel}) = \int |M^{(1)}(\mathbf{p}_1)|^2 d^2 p_{1\perp} \tag{13}$$

and

$$F^{(2)}(p_{2\parallel}) = \int |M^{(2)}(\mathbf{p}_2)|^2 d^2 p_{1\perp}, \tag{14}$$

where the partial transition amplitudes for the first and the second electron read

$$M^{(1)}(\mathbf{p}_1) = \int_{-\infty}^{\infty} dt'' \int_{t''}^{\infty} dt' \int d^3 k\, V_{\mathbf{p}_1,\mathbf{k}}^{(eg)} V_{\mathbf{k}}^{(g)} e^{i S_1(\mathbf{p}_1,\mathbf{k},t'',t')} \tag{15}$$

and

$$M^{(2)}(\mathbf{p}_2) = \int_{-\infty}^{\infty} dt\, V_{\mathbf{p}_2}^{(e)} e^{i S_2(\mathbf{p}_2,t)}, \tag{16}$$

respectively, and the transverse momentum components are integrated over. Note that, due to causality, the total ionization probabilities are not the product of such functions [20].

In Figs. 3 and 4, respectively, we display $F^{(1)}(p_{1\parallel})$ and $F^{(2)}(p_{2\parallel})$ computed for *each* of the contributions described in the previous section. For the first electron, Fig. 3 illustrates very clearly the loss of relevance in Pair 3($e_1$) discussed above as the
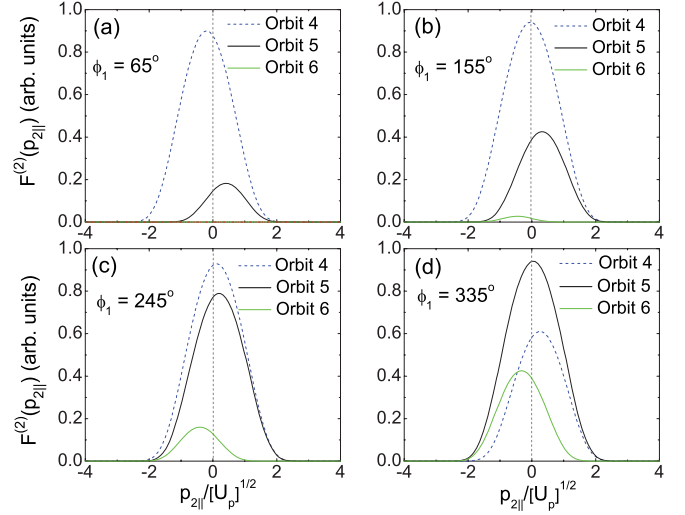


FIG. 4. (Color online) Partial electron momentum distributions $F^{(2)}(p_{2\parallel})$ [Eq. (14)] computed using the three most relevant individual ionization pathways for the second electron according to Fig. 2 and Table I, for the same field and atomic parameters as in the previous figure. From left to right, the phases $\phi_1 = 65°$ [panel (a)], $\phi_1 = 155°$ [panel (b)], $\phi_1 = 245°$ [panel (c)], and $\phi_1 = 335°$ [panel (d)] have been taken. The probability densities have been normalized to slightly below unity for the dominant contributions in each panel, in order to facilitate a more direct comparison. The dotted lines in panels (a) to (d) indicate the momentum $p_{2\parallel} = 0$, where the partial distributions related to a monochromatic driving field are expected to be peaked.

CEP increases [see Figs. 3(a) and 3(b)]. The contributions from such a pair, mostly located in the negative parallel momentum region, become vanishingly small already for $\phi_1 = 245°$. In fact, even for $\phi_1 = 65°$ this pair is not dominant, as the partial probability density associated with Pair 4($e_1$), mostly in the positive momentum region, is higher. This is a consequence of the fact that the field strength at the corresponding ionization time is higher for Pair 4($e_1$), so that the first electron tunnels through a narrower barrier (see Fig. 1). In Figs. 3(b) to 3(d), the partial momentum distributions also show that Pair 5($e_1$) is very important over a large CEP range and, in fact, provides the dominant ionization pathway for the first electron for $\phi_1 = 155°$ and $\phi_1 = 245°$ [see Figs. 3(b) and 3(c)]. This is in agreement with Fig. 1, which shows that, for a large range of phases, the instantaneous field at ionization is near its absolute maximum for this pair. In fact, only for $\phi_1 = 335°$ does Pair 6($e_1$) become dominant. Another interesting feature is that the curves corresponding to a specific Pair $n(e_1)$ are the mirror images of those related to Pair $n+1(e_1)$ if the CEP is shifted in $\Delta\phi = 180°$. This holds for all partial probabilities displayed in Figs. 3(a) to 3(d). For instance, $F^{(1)}(p_{1\parallel})$ for Pair 3($e_1$) in Fig. 3(a) is equal to $F^{(1)}(-p_{1\parallel})$ for Pair 4($e_1$) in Fig. 3(c), and so on. Finally, the peaks of the partial distributions agree with the predictions in Sec. III obtained from the solutions of the saddle-point equations.

For the second electron, the partial probabilities $F^{(2)}(p_{2\parallel})$ confirm that the main ionization channel is via Orbit 4($e_1$) for a large range of CEPs, as shown in Figs. 4(a) and 4(b). The contributions from Orbit 5($e_2$) only start to compete with this channel at $\phi_1 = 245°$, and eventually become dominant

TABLE I. Most relevant orbits for the first and second electrons for the values of the CEP employed in this work, in order of decreasing importance. A single number for more than one orbit indicates that their contributions are comparable or competing, while different numbers indicate the clear dominance of a pair for the first electron, or an orbit for the second electron. The signs ($\pm$) indicate whether a specific pair of orbits leads to electron momentum distributions $|F^{(1)}(p_{1\parallel})|^2$ peaked at positive ($+$) or negative ($-$) momentum. Subsequently, this will imply that the contributions triggered by such a pair of orbits will populate either the positive or the negative half axis in the parallel-momentum plane.

| $\phi_1$ (degrees) | First electron | Second electron |
|---|---|---|
| | 1. Pair 4 ($+$) | 1. Orbit 4 |
| 65 | 2. Pair 3 ($-$) | 2. Orbit 5 |
| | Pair 5 ($-$) | 3. Orbit 6 |
| | 1. Pair 5 ($-$) | 1. Orbit 4 |
| 155 | 2. Pair 4 ($+$) | 2. Orbit 5 |
| | 3. Pair 3 ($-$) | 3. Orbit 6 |
| | 1. Pair 5 ($-$) | 1. Orbit 4 |
| 245 | 2. Pair 4 ($+$) | Orbit 5 |
| | Pair 6 ($+$) | 2. Orbit 6 |
| | 1. Pair 6 ($+$) | 1. Orbit 5 |
| 335 | 2. Pair 5 ($-$) | 2. Orbit 4 |
| | 3. Pair 4 ($+$) | 3. Orbit 6 |

at $\phi_1 = 335°$ [Figs. 4(c) and 4(d), respectively]. One should note that the symmetry $F^{(2)}(p_{2\parallel})$ for Orbit $n(e_2)$ corresponds to $F^{(2)}(-p_{2\parallel})$ for Orbit $n+1(e_2)$ also occurs upon a phase shift $\Delta\phi_1 = 180°$. In the figure, however, it cannot be observed as Orbit $3(e_2)$ is missing. This orbit corresponds to ionization events triggered by Pairs $1(e_1)$ or $2(e_1)$, as illustrated in Figs. 1 and 2. Such pairs are irrelevant due to the weak field amplitudes involved [23]. In Table I we provide a summary of the most relevant orbits encountered for the first and second electrons in decreasing order of importance.

### B. Correlated electron momentum distributions

The fact that RESI is a correlated two-electron process implies that the shapes and regions populated by the NSDI electron momentum distributions will be determined by the interplay between the dominant contributions from the first and second electron.

In order to understand this issue, we compute the correlated electron-momentum distributions,

$$F(p_{1\parallel}, p_{2\parallel}) = \iint d^2 p_{1\perp} d^2 p_{2\perp} |M(\mathbf{p}_1, \mathbf{p}_2) + \mathbf{p}_1 \leftrightarrow \mathbf{p}_2|^2,$$

$$(17)$$

as functions of the momentum components $p_{n\parallel}$ ($n = 1, 2$) parallel to the laser-field polarization. In Eq. (17), unless otherwise stated, $M(\mathbf{p}_1, \mathbf{p}_2)$ is the transition amplitude (1) associated with the coherent sum of all processes over all sets of orbits, for both the first and the second electrons. These transition amplitudes are symmetrized to account for the fact that both electrons are indistinguishable. The transverse-momentum components are integrated over. These distributions are plotted in Fig. 5.
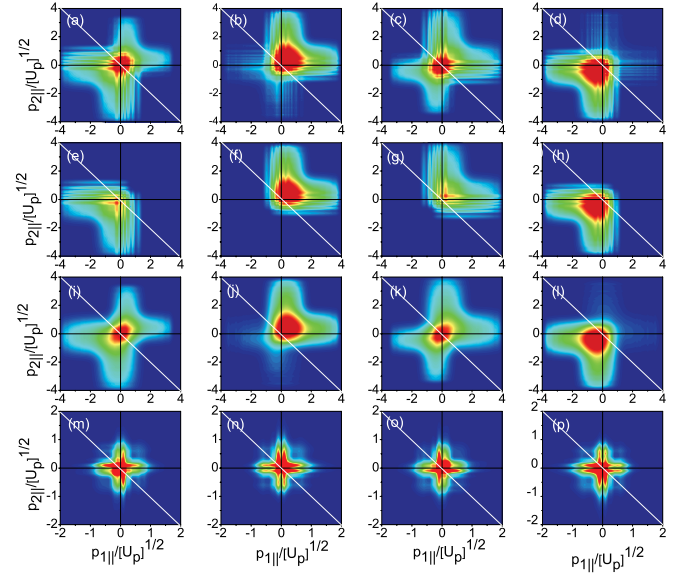


FIG. 5. (Color online) Correlated RESI electron momentum distributions as functions of the parallel momentum components $p_{1\parallel}$, $p_{2\parallel}$ for the same atomic and field parameters as in the previous figures. In panels (a) to (l), constant ionization and excitation prefactors $V_{\mathbf{p}_1 e, \mathbf{k}g}$, $V_{\mathbf{p}_2 e}$ prefactors have been employed, while in panels (m) to (p) the prefactors related to the excitation from a $3p$ to a $4s$ state by a contact type interaction have been used. The explicit expressions for these prefactors is given in Ref. [18]. From left to right, the CEPs are $\phi_1 = 65°$ [panels (a), (e), (i), and (m)], $\phi_1 = 155°$ [panels (b), (f), (j), and (n)], $\phi_1 = 245°$ [panels (c), (g), (k), and (o)], and $\phi_1 = 335°$ [panels (d), (h), (l), and (p)]. When constant prefactors are used, from the top to the bottom of the figure, we plot the distributions obtained as follows. Panels (a) to (d): all pairs of orbits for the first electron and all possible ionization pathways for the second electron displayed in Table I. Panels (e) to (h): all ionization channels for the second electron specified in Table I and Pair $3(e_1)$ [panel (e)], $4(e1)$ [panels (f) and (g)], and $5(e_1)$ [panel (h)] for the first electron. Panels (i) to (l): all pairs of orbits for the first electron specified in Table I, but only the ionization pathways for the second electron immediately after that specific ionization event, that is, Orbit $4(e_2)$ for Pair $3(e_1)$, Orbit $5(e_2)$ for Pair $4(e_1)$, and Orbit $6(e_1)$ for Pair $5(e_1)$. In panels (m) to (o), we have included all orbits for the first and second electron specified in Table I. For panels (a) to (l), the color scales range from 0 to $1 \times 10^{-5}$, while in panels (m) to (o) they range from 0 to $1 \times 10^{-20}$. The white lines in the figure indicate the antidiagonal $p_{1\parallel} = -p_{2\parallel}$.

For $\phi_1 = 65°$, the distributions occupies a broad region along the negative half axes $p_{i\parallel} = 0$ ($p_{j\parallel} < 0$), with $i \neq j$, as displayed in Fig. 5(a). This illustrates the importance of Pair $3(e_1)$, as a direct comparison with Fig. 5(e) shows. Even if this pair is not related to the most prominent ionization event for the second electron, upon rescattering, it triggers the dominant tunnel ionization channel for the second electron, that is, along Orbit $4(e_2)$. This counterbalances the influence of Pair $4(e_1)$, which, according to the partial distributions in Fig. 3 and our previous line of argument, is the prevalent ionization pathway for the first electron for this specific CEP value. Contributions from Pair $4(e_1)$ along the parallel momenta positive half axes are also present. These contributions are, however, comparable, or even slightly weaker, as rescattering

along Pair 4($e_1$) can only lead to ionization along Orbit 5($e_2$), Orbit 6($e_2$), or even later orbits. Furthermore, because an electron returning along Pair 3($e_1$) acquires a higher kinetic energy than if it returns along Pair 4($e_1$), the momentum region populated by events related to former pair is larger. This fact is also observed for the partial momentum distribution in Fig. 3(a), which exhibits comparable probability densities over a broad momentum region for Pair 3($e_1$).

For $\phi = 155°$, in contrast, Pair 4($e_1$) prevails [see Figs. 5(b) as compared to 5(f)]. This leads to a shift in the distribution towards the positive half axis of the $p_{1\parallel} p_{2\parallel}$ plane. Physically, this can be attributed to the loss of relevance related to Pair 3($e_1$), together with the fact that the ionization channel along Orbit 5($e_2$) becomes more prominent. Hence, ionization along Orbit 4($e_2$) can no longer counterweight the other effects. This is in agreement with the previous discussions in Sec. III and Figs. 3 and 4. Note, however, that the partial probability density $F^{(1)}(p_{1\parallel})$ associated with Pair 5($e_1$) is dominant in Fig. 3(b). Nevertheless, Pair 5($e_1$) can only lead to ionization events related to Orbit 6($e_2$) or later. These events are too close to the pulse turnoff to play a significant role.

The distributions obtained for $\phi_1 = 245°$ [Fig. 5(c)], on the other hand, show that, as the CEP increases, Pair 5($e_1$) becomes more relevant and starts to influence the overall distributions. For this specific phase, the ionization channel for the first electron along Pair 3($e_1$) is negligible, regardless of the subsequent ionization events. Ionization along Pair 4($e_1$) is relatively small. It may, however, cause ionization of the second electron along Orbit 5($e_1$), which is quite prominent. Pair 5($e_1$) is the most prominent ionization channel for the first electron, but may lead to ionization only along Orbit 6($e_2$) or at later times. Hence, Pair 4($e_1$), whose contributions are presented in Fig. 5(g), still determines the momentum regions to be occupied. Interestingly, this distribution is the mirror image of that obtained for $\phi_1 = 65°$ with regard to $(p_{1\parallel}, p_{2\parallel}) \rightarrow (-p_{1\parallel}, -p_{2\parallel})$.

Finally, for $\phi_1 = 335°$, displayed in Fig. 5(d), the distributions are almost entirely concentrated along the negative half axis $p_{i\parallel} = 0$ ($p_{j\parallel} < 0$), with $i \neq j$. This is a consequence of the fact that, together, the pathways related to Pair 5($e_1$) for the first electron and Orbit 6($e_2$) for the second electron determine the momentum regions to be populated [see Fig. 5(h) for comparison]. A similar interpretation provided when discussing the distributions obtained in Fig. 5(b), for $\phi_1 = 155°$, applies, with the difference that all the indices must be shifted by 2; that is, instead of Pairs 3($e_1$) and 4($e_1$), now one must consider Pairs 5($e_1$) and 6($e_1$) and the subsequent orbits for the second electron. Note once more that this distribution is the mirror image of that depicted in Fig. 5(b).

Apart from the effects discussed above, throughout, there exist residual fringes parallel to the axis $p_{n\parallel} = 0$. These fringes are related to the fact that, in our computations, we have included all the relevant orbits along which the second electron may tunnel, subsequently to being excited by a particular pair of orbits. Quantum mechanically, the transition amplitudes related to these pathways interfere and even partly survive the integration over the transverse momentum components. In a more realistic scenario, however, we expect these fringes to be absent, due to the fact that the excited bound state from which the second electron is released is strongly depleted. Hence,
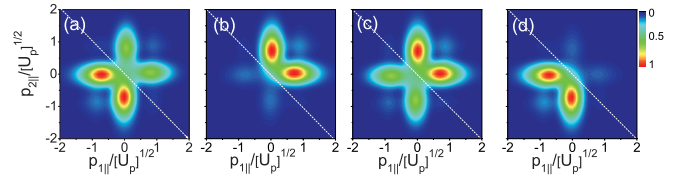


FIG. 6. (Color online) Correlated RESI electron momentum distributions as functions of the parallel momentum components $p_{1\parallel}$, $p_{2\parallel}$ for the same atomic parameters as in the previous figures, but a much lower peak-field intensity ($I = 1.5 \times 10^{14}$ W/cm$^2$). Throughout, we have considered the prefactors $V_{\mathbf{p}_{1e},\mathbf{k}g}$ related to the excitation from a $3p$ to a $4s$ state by a contact-type interaction and only the first tunnel ionization events after rescattering of the first electron. Panels (a), (b), (c), and (d) correspond to the CEPs $\phi_1 = 65°$, $\phi_1 = 155°$, $\phi_1 = 245°$, and $\phi_1 = 335°$, respectively. The white lines in the figure indicate the antidiagonal $p_{1\parallel} = -p_{2\parallel}$. In order to highlight the difference in probability density between the maxima and the region around the origin $p_{1\parallel} = p_{2\parallel} = 0$, we have normalized the color scales to unity (originally they extended from zero up to roughly $1 \times 10^{-21}$).

ionization would mainly occur around the field maximum closest to the time of excitation.

In order to mimic depletion, in Figs. 5(i) to 5(l) we consider only this ionization pathway. As an overall feature, the above-mentioned structure disappears. Furthermore, the correlated probability densities are now slightly displaced from the axes $p_{n\parallel} = 0$. This occurs because, due the lack of monochromaticity of the few-cycle pulse, Im[$\omega t$] no longer exhibits a minimum at $p_{\parallel} = 0$ (see discussion in Sec. III). If many ionization events are considered, this effect tends to average out and this asymmetry is less prominent [24]. Finally, in Figs. 5(m) to 5(p) we incorporate the prefactors $V_{\mathbf{p}_{1g},\mathbf{k}g}$ and $V_{\mathbf{p}_{2e}}$ corresponding to an excitation process from the $3p$ to the $4s$ state a contact-type interaction $V_{12}(\mathbf{r}_1,\mathbf{r}_2) = \delta(\mathbf{r}_1 - \mathbf{r}_2)$. For the explicit expressions, see Ref. [18]. In general, these prefactors introduce a bias towards low momenta, so that the distributions are much more focused around the origin $p_{1\parallel} = p_{2\parallel} = 0$. For a Coulomb-type interaction $V_{12} = 1/|\mathbf{r}_2 - \mathbf{r}_1|$, we have verified that even lower momenta are favored. This would imply that, for this parameter range, including the prefactors almost washes away the CEP dependence.

We have found, however, that if much lower peak intensities are taken, the region around $p_{1\parallel} = p_{2\parallel} = 0$ becomes much less populated and the CEP dependence obtained in our model resembles much more that reported in Ref. [15]. This behavior is displayed in Fig. 6. In the figure, one may identify two sets of peaks at $(p_{i\parallel}, p_{j\parallel}) = (\pm\sqrt{U_p}, 0)$, which, depending on $\phi_1$, are located at either the positive or the negative half axis. This location changes according to the dominant events for the first and second electrons. In fact, the whole interplay between the rescattering and ionization events remains as discussed above. The main difference is that the momentum range determined by excitation constraint (10), that is, the "length" of the cross-shaped structure, is much smaller, and does not reach up to the origin. The fact that peaks are not located near $-A(t')$, but at a much lower momentum, comes from the $3p \rightarrow 4s$ excitation prefactor, which exhibits maxima in this region. This prefactor also guarantees that the distributions are well localized along the axis (see Ref. [18] for details). Another noteworthy feature is that, in the figure, we have employed

only the ionization event closest in time to the rescattering of the first electron. If more events are taken, a set of fringes is obtained, corresponding to the interference of several tunnel ionization events (not shown). This illustrates the importance of depletion.

## V. CONCLUSIONS

In this work, we highlight the influence of the CEP for the RESI pathway in NSDI with few-cycle pulses. The electron-momentum distributions are quite sensitive with regard to the CEP, and, as this parameter varies, move from the region below to the region above the antidiagonal $p_{1\parallel} = -p_{2\parallel}$, or vice versa, in the plane spanned by the electron-momentum components parallel to the laser field polarization. Similarly to our previous studies in Refs. [7,8] performed for the simpler NSDI mechanism of electron-impact ionization, we show that all features encountered can be explained in terms of electron trajectories. Indeed, a detailed analysis of where these trajectories are located within the pulse and, in the context of the steepest descent method, of the real and imaginary parts of the ionization times of both electrons and the rescattering time of the first electron provides a consistent picture related to the shapes, maxima, and regions populated by the RESI electron-momentum distributions. All such features are determined by the interplay between the dominant sets of trajectories for the first and second electrons.

Qualitatively, the results in the present publication agree with those observed experimentally in Ref. [15] only if much lower driving-field intensities are taken, namely of the order of the half of that reported in Ref. [15]. In this case, the shapes of the electron-momentum distributions bear a reasonable resemblance to the experimental findings and, depending on the CEP, shift from the region below to the region above the antidiagonal $p_{1\parallel} = -p_{2\parallel}$. This is especially true if we consider the prefactors $V_{\mathbf{p}_2 e}$, $V_{\mathbf{p}_1 e,\mathbf{k}g}$ associated with an excitation from the $3p$ to the $4s$ state in argon and include only the tunneling event for the second electron immediately after the collisional excitation took place. In contrast, if the intensities in Ref. [15] are taken, we find a much larger probability density around the origin $p_{1\parallel} = p_{2\parallel} = 0$. This central feature is absent in the experiments and, if the prefactors corresponding to the $3p$ to $4s$ excitation are included, the CEP dependence is almost washed out.

These discrepancies may be related to several issues, all of which would considerably affect the constraint (10) for the momentum of the first electron upon rescattering, and hence the regions populated by the electron-momentum distributions. First, there is always an uncertainty in the experimentally measured peak intensities. If this intensity is smaller than that employed in our computations, this means that the region around $p_{1\parallel} = p_{2\parallel} = 0$ is less populated than in Fig. 5 (see [18,19] for details). Second, in a more realistic scenario, it may be that excitation to higher-lying states also occurs. This would increase the energy difference $E_{\text{exc}}$ between the ground and excited states of singly ionized argon, and thus reduce the classically allowed region. Third, the momentum constraints related to the first and second electrons, which have been derived within the context of the strong-field approximation [18,20], neglect the presence of the binding potential when the

electron is in the continuum. It could well be that the Coulomb potential has a strong influence in the momenta with which the first electron returns to the core, if it is sufficiently slow, that is, near the origin of the $p_{1\parallel} p_{2\parallel}$ plane.

Finally, we would like to comment on the role of depletion on the RESI electron-momentum distributions. In Ref. [15], the probability densities at nonvanishing momenta which led to the axes of the cross have been attributed to the second electron. It has been argued that, due to depletion, the second electron left before the peak field with nonvanishing momentum. Our results, together with the constraints stated in this paper, suggest that depletion will mainly shift the probability density with regard to the axis $p_{n\parallel} = 0$ [see discussion of panels (i) to (l) in Fig. 5]. This effect, however, seems to be relatively small. According to our model, the shift in the probability density away from the origin $p_{1\parallel} = p_{2\parallel}$ is mainly caused by the first electron, which, upon recollision, acquires the additional momentum $-A(t)$ from the field according to the constraints stated in Sec. II. A more important effect is that the lack of depletion would introduce several ionization events subsequent to excitation, which, quantum mechanically, would interfere. This would lead to fringes in the electron-momentum distributions. The issue of depletion and the role of the Coulomb potential are not yet fully understood and will be pursued in future work.

## APPENDIX: QUANTUM-ORBIT ANALYSIS

In this Appendix, we perform a quantum-orbit analysis of the problem, with emphasis on how the dominant sets of orbits change with the CEP. The concept of "quantum orbits" is based on the fact that the solutions of the saddle-point equations can be related to the classical orbits of an electron in a field and still retain information on quantum aspects such as tunneling and interference (for a broad overview, see [25]).

### 1. First electron

We start by focusing on the first electron, for which the saddle-point equations (6)–(8) give the complex ionization and rescattering times. We study Pairs $3(e_1)$, $4(e_1)$, and $5(e_1)$, as, for a wide range of CEPs, such pairs are expected to lead to the most relevant contributions for the specific pulse chosen. For the cases studied in this section, the saddle-point solutions have been obtained for vanishing momenta $p_{1\perp}$ and different CEP values.

Figure 7 displays the real and imaginary parts of the above-mentioned solutions, for Pair $3(e_1)$. As an overall feature, the real parts of the ionization and return times are centered around $p_{1\parallel} = -A(t')$, which is in the negative parallel momentum region [see Figs. 7(a) and 7(b), respectively]. This is the most probable momentum for the first electron upon rescattering. Furthermore, $\text{Re}[\omega t'']$ and $\text{Re}[\omega t']$ almost coalesce at two
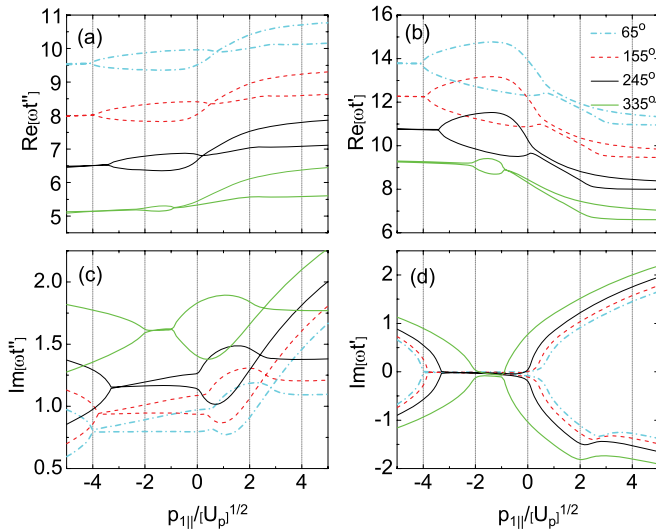
FIG. 7. (Color online) Real and imaginary parts of the complex ionization and rescattering times $t''$ and $t'$ of the first electron obtained from the solutions of the saddle-point equations (6)–(8) corresponding to Pair 3 in Fig. 1 for vanishing transverse momentum $p_{1\perp} = 0$. Panels (a) and (b) give the real parts of such solutions, and panels (c) and (d) give the imaginary parts. The bound-state energies correspond to argon assuming a $3p \rightarrow 4s$ excitation ($E_{1g} = 0.58$ a.u., $E_{2g} = 1.02$ a.u., and $E_{2e} = 0.40$ a.u.) in a few-cycle pulse of frequency $\omega = 0.06085$ a.u. and intensity $I = 3 \times 10^{14}$ W/cm$^2$. The CEPs $\phi_1$ employed are indicated in the figure.

specific values of the parallel momentum components $p_{1\parallel}$. These are the minimum and the maximum momentum values for which rescattering exhibits a classical counterpart. Outside this region, this process is forbidden and the corresponding transition amplitude is exponentially decaying.

The figure shows that the ionization and rescattering times, the center, and the extension of the classically allowed region strongly depend on the CEP. In particular, there is a very good agreement between the center of the region shown in Figs. 7(a) and 7(b) and the ionization and return times indicated by arrows in Fig. 1, which were identified employing classical arguments. As the CEP increases, the real parts of such times move towards the pulse turn on. This will lead to a decrease in the extension of the classically allowed region from $-4\sqrt{U_p} \leqslant p_{1\parallel} \leqslant 0.7\sqrt{U_p}$ for $\phi_1 = 65°$ to $-2\sqrt{U_p} \leqslant p_{1\parallel} \leqslant -0.8\sqrt{U_p}$ for $\phi_1 = 335°$. This can be physically understood by direct inspection of Fig. 1 and by bearing in mind that the classical limit of the kinetic energy of the first electron upon return is given by $E_{\text{kin}}^{(\text{cl})} = [A(t') - A(t'')]^2/2$ [26]. For $\phi_1 = 65°$, at the ionization time related to Pair 3($e_1$), $A(t'') \simeq 0$, and, at the rescattering time, the vector potential $A(t')$ is around its peak value $A_0$. Hence, the kinetic energy of the first electron upon return is high. This implies that, for this phase, the contributions of Pair 3($e_1$) will populate a large momentum region. As the CEP is increased up to $\phi_1 = 335°$, the instantaneous vector potential $A(t')$ decreases to less than $0.8A_0$. Furthermore, due to the lack of monochromaticity of the field, $A(t'')$ is no longer vanishing near the pulse turn on. Both effects lead to a decrease in this momentum region. Apart from that, the center of the classically allowed region, which is

determined by the most probable momentum the electron may have upon return, moves from roughly $-2\sqrt{U_p}$ to $-1.4\sqrt{U_p}$. This is due to the fact that, close to the peak of the pulse, the former value is a good approximation for $-A(t')$, while, near the edges of the pulse, its lack of monochromaticity plays an increasingly important role.

The imaginary parts of $t''$ and $t'$, shown in the remaining panels of Fig. 7, give valuable information on whether the process in question is allowed or forbidden or on the overall probability related to a specific process, for example, tunneling ionization. For instance, Im[$\omega t''$], displayed in Fig. 7(d), sheds some light on how the width of the potential barrier that the electron must overcome in order to reach the continuum varies for Pair 3($e_1$), with regard to the CEP. The larger Im[$\omega t''$] is, the wider is the potential barrier through which the electron must tunnel [27]. The picture shows a marked increase in Im[$t''$] as the CEP varies from $\phi_1 = 65°$ to $\phi_1 = 335°$. This can be understood with the help of Fig. 1. According to this figure, for $\phi_1 = 65°$, the first electron tunnels near a local maximum for which the instantaneous electric field is $0.8E_0$. As the CEP increases, the local maximum associated with tunnel ionization for Pair 3($e_1$) decreases down to less than $0.4E_0$ for $\phi_1 = 335°$. Hence, the potential barrier widens and the contributions of this specific pair become less and less relevant. Note that Im[$\omega t''$] $\neq 0$ throughout, as tunneling is not classically allowed.

Finally, Fig. 7(d) shows the behavior of Im[$\omega t'$], which is associated to the rescattering time, with regard to the CEP. In contrast to what happens to Im[$\omega t''$], this imaginary part vanishes at the momentum range between the values of $p_{1\parallel}$ for which Re[$\omega t''$] and Re[$\omega t'$] almost coalesce. This is related to the fact that, in this region, rescattering is classically allowed. This region decreases in extension for increasing values of $\phi_1$. Once more, this reflects the fact that Pair 3($e_1$) loses relevance.

The above-mentioned loss of relevance does not happen to all pairs of orbits, but will depend strongly on how the corresponding start and return times are located within the pulse. In fact, it may occur that, as the CEP increases, a specific set of trajectories becomes dominant, or even remains relatively stable. In order to understand this issue, it suffices to analyze the real and imaginary parts of the ionization time $t''$. An example is provided in Fig. 8 for Pair 4($e_1$) and Pair 5($e_1$). The contributions of the former pair to the NSDI distributions remain relatively stable, while the latter pair increases in relevance within the CEP range studied. The real and imaginary parts of the complex ionization time $t''$ are depicted in Fig. 8 for both orbits.

Figure 8(a) shows that, for Pair 4($e_1$), the classically allowed region, centered at a positive parallel momentum, remains roughly the same throughout. This happens because the absolute value of the vector potential $A(t')$, and hence the kinetic energy obtained by the electron upon return, remains quite large for the CEP range studied. The behavior of Pair 5($e_1$), however, displayed in Fig. 8(b), is markedly different. For this pair, the extension of the classically allowed region increases substantially as the CEP increases. This is expected as, in this case, the approximate ionization and rescattering times in Fig. 1 move from the turn off to the center of the pulse with increasing CEP. Consequently, the vector potential $A(t')$ at the instant of rescattering increases from approximately
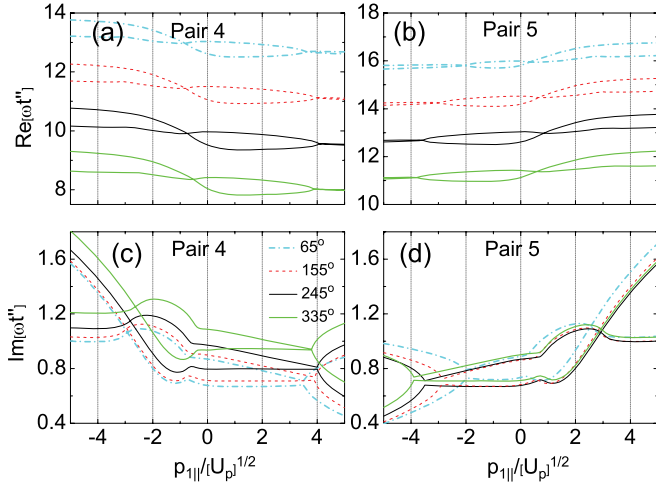
FIG. 8. (Color online) Real and imaginary parts of the complex ionization times $t''$ of the first electron obtained from the solutions of the saddle-point equations (6)–(8) corresponding to Pairs 4 and 5 in Fig. 1, for vanishing transverse momentum $p_{1\perp} = 0$. Panels (a) and (b) give the real parts of such solutions, and panels (c) and (d) give the imaginary parts. The field and atomic parameters are the same as in the previous figures.

$0.4A_0$ to $A_0$. This leads to a substantial increase in the electron kinetic energy upon return.

Another important issue determining the dominance of a pair of orbits is the width of the potential barrier through which the first electron tunnels, which can be roughly inferred from $\text{Im}[\omega t'']$. For Pair $4(e_1)$, $\text{Im}[\omega t'']$ remains relatively stable throughout, as shown in Fig. 8(c). An inspection of Fig. 1 shows that, indeed, the instantaneous electric field strength $|E(t'')|$ related to Pair $4(e_1)$ is rather large. Hence, one expects the corresponding potential barrier to be quite narrow. For increasing CEP, $\text{Im}[t'']$ increases slightly. This is due to the fact that $\text{Re}[\omega t'']$ related to this pair moves towards the pulse turn on and the potential barrier at the ionization time $t''$ becomes slightly wider. A similar analysis can be performed in the imaginary parts of the saddle-point solutions for Pair $5(e_1)$. Figure 8(d) shows that such imaginary parts are comparable to those observed for Pair $4(e_1)$ for a wide range of phases. Hence, we expect both sets of orbits to compete, until Pair $5(e_1)$ becomes dominant.

### 2. Second electron

For the second electron, a set of orbits will be dominant only if it is excited in such a way that its subsequent tunneling probability is high. In order to obtain this information, we look at the tunnel ionization times of the second electron, which can be obtained by solving the saddle-point equation (9). The real and imaginary parts of these solutions are displayed in Fig. 9 (upper and lower rows, respectively), for vanishing transverse momentum $p_{2\perp} = 0$. We only consider Orbits $n(e_2)$ for $n$ ranging from 4 to 7. The preceding orbits, that is, Orbits $n(e_2)$ with $n = 1, 2, 3$, will not play an important role, as they violate causality with regard to Pair $3(e_1)$. Note that, for the second electron, the orbits are well separated for all momentum ranges. There is also no classically allowed region, as tunneling is an intrinsically quantum mechanical phenomenon. Hence,
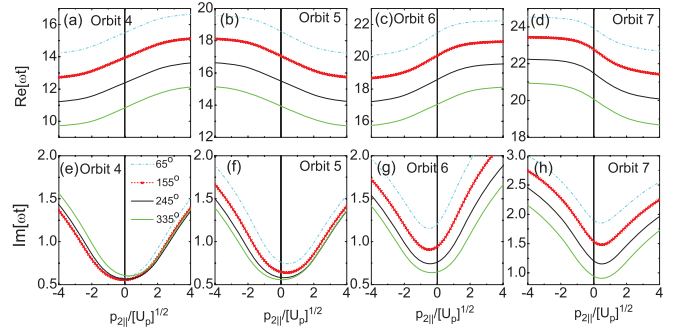


FIG. 9. (Color online) Real and imaginary parts of the complex ionization times $t$ of the second electron obtained from the solutions of the saddle-point equation (9) corresponding to Orbits 4 to 7 in 2, for vanishing transverse momentum $p_{2\perp} = 0$. Panels (a) to (d) give the real parts of such solutions, while panels (e) to (h) depict the imaginary parts.

$\text{Im}[\omega t] \neq 0$ throughout. Once more, one may draw an intuitive picture by relating the solutions in Fig. 9 to the simplified arguments illustrated in Fig. 2.

For all phases, we observe that, for parallel momentum $p_{2\parallel} \simeq 0$, $\text{Re}[\omega t]$ corresponds to the times for which the pulse has local extrema, marked by the rectangles in Fig. 2. These extrema vary from the center until the pulse turnoff and correspond to the most probable ionization times for the second electron, that is, when the potential barrier is narrowest for a specific orbit. A maximal ionization probability near $p_{2\parallel} = 0$ and its relation to the narrowest potential barrier can also be inferred by inspecting $\text{Im}[\omega t]$, which exhibits a minimum around this value (see lower row in the figure). The above-stated features, that is, the electron tunneling most probably at peak fields and a corresponding minimum at $\text{Im}[t]$ at such times, are also observed for a monochromatic field [19].

However, due to the lack of monochromaticity in the pulse, there are sometimes small deviations from $p_{2\parallel} = 0$, especially if the orbits are near the pulse turnon and turnoff. This feature can be seen very clearly, for instance, in Fig. 9(h), which corresponds to a tunnel ionization event close to the pulse turnoff, that is, to Orbit $7(e_2)$. Furthermore, $\text{Im}[\omega t]$ is not symmetric with regard to its value at $p_{2\parallel} = 0$. This would be the case for a monochromatic field, as all cycles, and hence the regions around each local field maximum, would be identical for a continuous wave [19]. In a few-cycle pulse, however, one expects the potential barrier through which the second electron must tunnel to narrow, or to widen, as the ionization times approach or distance themselves from the center of the pulse, respectively. This leads to asymmetries in $\text{Im}[\omega t]$ for positive and negative momenta. In the specific pulse discussed in this work, for Orbits $5(e_2)$ and $7(e_2)$ [Figs. 9(f) and 9(h), respectively], $\text{Im}[\omega t]$ decreases for $p_{2\parallel} > 0$, in comparison to the region for which $p_{2\parallel} < 0$, while, for Orbit $6(e_2)$, the opposite behavior holds. This asymmetry can be understood by inspecting the respective upper panels, together with Fig. 2. For Orbits $5(e_2)$ and $7(e_2)$, if the electron leaves before the corresponding field maxima, its momentum will be positive [see Figs. 9(b) and 9(d), respectively]. An inspection of Fig. 2 shows that these temporal regions are located closer to the center of the pulse, compared to the time regions subsequent

to the local field maxima. In contrast, for Orbit 6($e_2$), earlier ionization times, and a larger proximity to the central region of the pulse, correspond to negative momenta. For orbit 4($e_2$), the above-mentioned asymmetry varies, as shown in Fig. 9(e). This happens because, throughout, the ionization times are very close to the pulse center. Hence, whether ionization times prior or subsequent to the local maxima will correspond to higher or lower local field intensities will depend on the CEP.

The dominant sets of orbits in a few-cycle pulse can be identified by analyzing Fig. 9. As a general feature, as $\phi_1$ increases, the real parts of the ionization times move towards lower values, as shown in Figs. 9(a)–9(d). This is consistent with Fig. 2 and with the previous analysis, performed for the first electron. Some orbits, such as Orbits 5($e_2$)–7($e_2$), move towards the center of the pulse, while others, such as Orbit 4($e_2$), move away from it. This behavior, and its consequences for the shape of the electron-momentum distributions, can be inferred by analyzing the imaginary parts of the ionization times, displayed in Figs. 9(e)–9(h). These panels show that the most important orbits for the second electron will be Orbits 4($e_2$) and 5($e_2$). This is due to the fact that, for these orbits,

near $p_{2\parallel} = 0$, $0.5 \leqslant \text{Im}[\omega t] \leqslant 0.75$, while, for the remaining orbits, $\text{Im}[\omega t]$ is, in general, larger. This implies that the potential-energy barriers through which the electron must tunnel are narrower for Orbits 4($e_2$) and 5($e_2$). Interestingly, $\text{Im}[\omega t]$ remains stable for Orbit 4($e_2$) throughout. This may be understood by inspecting the local maximum of $E(t)$ in Fig. 2 related to this orbit. The figure shows that the instantaneous field strength at this maximum remains located near $0.8E_0$ for the CEP range considered. In contrast, for Orbit 5($e_2$), $\text{Im}[\omega t]$ decreases systematically from around 0.75 to 0.5 as the phase varies from from $\phi_1 = 65°$ to $\phi_1 = 335°$ [see Fig. 9(f)]. This occurs because the instantaneous field strength $|E(t)|$ related to this orbit increases from less than $0.5E_0$ to almost the full amplitude $E_0$ in this phase interval, as shown in Fig. 2.

For the remaining pairs of orbits, there is always a decrease in $\text{Im}[\omega t]$ with regard to increasing CEP values. This is due to the fact that the real parts of such times move from the pulse turn off towards the center of the pulse, so that the effective potential barrier becomes narrower. In particular, we expect vanishingly small contributions throughout for Orbit 7($e_2$), as in this case $\text{Im}[\omega t]$ is much larger than for the other orbits.

---

[1] See, e.g., T. Brabec and F. Krausz, Rev. Mod. Phys. **72**, 545 (2000), for a comprehensive review on this topic.

[2] S. Zherebtsov, T. Fennel, J. Plenge, E. Antonsson, I. Znakovskaya, A. Wirth, O. Herrwerth, F. Süßmann, C. Peltz, I. Ahmad, S. A. Trushin, V. Pervak, S. Karsch, M. J. J. Vrakking, B. Langer, C. Graf, M. I. Stockman, F. Krausz, E. Rühl, and M. F. Kling, Nat. Phys. **7**, 656 (2011).

[3] M. Schnürer, Ch. Streli, P. Wobrauschek, M. Hentschel, R. Kienberger, Ch. Spielmann, and F. Krausz, Phys. Rev. Lett. **85**, 3392 (2000); M. Henstchel, R. Kienberger, Ch. Spielmann, G. A. Reider, N. Milosevic, T. Brabec, P. B. Corkum, U. Heinzmann, M. Drescher, and F. Krausz, Nature (London) **414**, 509 (2001); Yunquan Liu, X. Liu, Y. Deng, C. Wu, H. Jiang, and Q. Gong, Phys. Rev. Lett. **106**, 073004 (2011); P. von den Hoff, I. Znakovskay, M. F. Kling, and R. de Vivie-Riedle, Chem. Phys. **366**, 139 (2009).

[4] G. Sansone, E. Benedetti, F. Calegari, C. Vozzi, L. Avaldi, R. Flammini, L. Poletto, P. Villoresi, C. Altucci, R. Velotta, S. Stagira, S. De Silvestri, and M. Nisoli, Science **314**, 443 (2006).

[5] F. Ferrari, F. Calegari, M. Lucchini, C. Vozzi, S. Stagira, G. Sansone, and M. Nisoli, Nat. Photon. **4**, 875 (2010); M. Schultze, E. Goulielmakis, M. Uiberacker, M. Hofstetter, J. Kim, D. Kim, F. Krausz, and U. Kleineberg, New J. Phys. **9**, 243 (2007).

[6] G. G. Paulus, F. Grasbon, H. Walther, P. Villoresi, M. Nisoli, S. Stagira, E. Prior, and D. Silvestri, Nature (London) **414**, 182 (2001); D. B. Milošević, G. G. Paulus, and W. Becker, Phys. Rev. Lett. **89**, 153001 (2002).

[7] X. Liu and C. Figueira de Morisson Faria, Phys. Rev. Lett. **92**, 133006 (2004).

[8] C. F. Faria, X. Liu, A. Sanpera, and M. Lewenstein, Phys. Rev. A **70**, 043406 (2004).

[9] C. Ruiz, L. Plaja, L. Roso, and A. Becker, Phys. Rev. Lett. **96**, 053001 (2006).

[10] Q. Liao, P. Lu, Q. Zhang, W. Hong, and Zh. Yang, J. Phys. B **41**, 125601 (2008).

[11] W. Quan, X. Liu, and C. Figueira de Morisson Faria, J. Phys. B **42**, 134008 (2009).

[12] S. Micheau, Zh. Chen, A.-Th. Le, and C. D. Lin, Phys. Rev. A **79**, 013417 (2009).

[13] X. Liu, H. Rottke, E. Eremina, W. Sandner, E. Goulielmakis, K. O. Keeffe, M. Lezius, F. Krausz, F. Lindner, M. G. Schätzel, G. G. Paulus, and H. Walther, Phys. Rev. Lett. **93**, 263001 (2004).

[14] N. Camus, B. Fischer, M. Kremer, V. Sharma, A. Rudenko, B. Bergues, M. Kübel, N. G. Johnson, M. F. Kling, T. Pfeifer, J. Ullrich, and R. Moshammer, Phys. Rev. Lett. **108**, 073003 (2012).

[15] B. Bergues, M. Kübel, N. G. Johnson, B. Fischer, N. Camus, K. J. Betsch, O. Herrwerth, A. Senftleben, A. M. Sayler, T. Rathje, I. Ben-Itzhak, R. R. Jones, G. G. Paulus, F. Krausz, R. Moshammer, J. Ullrich, and M. F. Kling, Nat. Commun. **3**, 817 (2012).

[16] B. Feuerstein, R. Moshammer, D. Fischer, A. Dorn, C. D. Schroter, J. Deipenwisch, J. R. Crespo Lopez-Urrutia, C. Hohr, P. Neumayer, J. Ullrich, H. Rottke, C. Trump, M. Wittmann, G. Korn, and W. Sandner, Phys. Rev. Lett. **87**, 043003 (2001).

[17] C. Figueira de Morisson Faria and X. Liu, J. Mod. Opt. **58**, 1076 (2011).

[18] T. Shaaran, M. T. Nygren, and C. Figueira de Morisson Faria, Phys. Rev. A **81**, 063413 (2010).

[19] T. Shaaran and C. Figueira de Morisson Faria, J. Mod. Opt. **57**, 984 (2010).

[20] T. Shaaran, C. Figueira de Morisson Faria, and H. Schomerus, Phys. Rev. A **85**, 023423 (2012).

[21] The length-to-velocity-gauge transformation will introduce a shift $\mathbf{p} \rightarrow \mathbf{p} - \mathbf{A}(t)$. This shift will effectively cancel out with the field dressing in the Volkov states which exists in the velocity gauge and will influence the ionization prefactors for the first and second electron. However, as tunnel ionization occurs close to the peak of the field, $A(t'') \simeq 0$ in the length-gauge prefactor (3) and $A(t) \simeq 0$ in the length-gauge prefactor (5). Hence, this will have little influence in practice.

[22] C. Figueira de Morisson Faria, H. Schomerus, and W. Becker, Phys. Rev. A **66**, 043413 (2002).

[23] The probability density associated with Pair 2($e_1$) for $\phi_1 = 65°$ is the mirror image of that related to Pair 3($e_1$) for $\phi = 245°$. We have verified that both rescattering events lead to a vanishingly small probability density.

[24] Concretely, the upper parts of the distributions in Fig. 5 are slightly displaced towards the first quadrant of the parallel momentum place. This is caused by the fact that ionization along Orbit 5($e_2$), which is the main ionization channel for the second electron related to Pairs 4($e_1$) and 6($e_1$), is favored for positive momenta [see Fig. 8(f)] and subsequent discussion in the Appendix). In contrast, the lower parts of such distributions are slightly shifted towards the third quadrant. This is due to the

fact that the main ionization channel for the second electron in this momentum region is either along Orbit 4($e_2$) ($\phi_1 = 65°$ and $\phi_1 = 155°$) or along Orbit 6($e_2$) ($\phi_1 = 245°$ and $\phi_1 = 335°$). For both orbits, ionization is slightly enhanced for negative momenta, as shown in Figs. 8(e) and 8(g).

[25] P. Salières, B. Carré, L. Le Déroff, F. Grasbon, G. G. Paulus, H. Walther, R. Kopold, W. Becker, D. B. Milošević, A. Sanpera, and M. Lewenstein, Science **292**, 902 (2001).

[26] Note that if the bound-state energy $E_1^{(g)} \to 0$, that is, in the classical limit, the saddle-point equation (6) gives $\mathbf{k} = -\mathbf{A}(t'')$.

[27] Roughly speaking, the tunneling amplitude is proportional to $\exp\{-\text{Im}[t'']\}$. If, for instance, $\text{Im}[t'']$ increases by a factor of two, this means that there will be a decrease in two orders of magnitude in this amplitude.